Corrosion performance of medical grade NiTi after laser processing

A. Michael [a],*, A. Pequegnat [a], J. Wang [a], Y.N. Zhou [a], M.I. Khan [b]

[a] Centre for Advanced Materials Joining (CAMJ), Department of Mechanical and Mechatronics Engineering, University of Waterloo, 200 University Avenue West, Waterloo, ON N2L 3G1, Canada
[b] Smarter Alloys Inc., 75 Bathurst Drive, Waterloo, ON N2V1N2, Canada

ARTICLE INFO

ABSTRACT

Laser processing of shape memory alloys (SMAs) has great potential to enable the multi-functionality required for complex applications. Achieving this improved functionality often requires laser processing of the SMA's with a high-energy pulse coupled with an observable decrease in the corrosion resistance, however there are discrepancies in the post-processing corrosion performance. The current study conducts a systematic investigation of Ni-44.2 wt% Ti SMA with differing numbers of laser pulses and post-process surface treatments. The localized electrochemical characteristics were investigated by scanning electrochemical microscopy. X-ray photoelectron spectroscopy and Raman spectroscopy was used to determine surface composition and oxide crystallinity, while oxide stability was determined via potentiodynamic cyclic polarization. Results showed that fewer pulses were not significantly detrimental to the corrosion performance. However, increasing the number of pulses had a significant impact on oxide stability in the heat affected zone due to increased crystallinity. The post-process surface treatments restored corrosion performance to pre-processed capabilities; however, further optimization is required to achieve maximum corrosion resistance.

© 2017 Elsevier B.V. All rights reserved.

1. Introduction

The shape memory effect (SME), pseudoelastic effect (PE), and outstanding mechanical properties of NiTi shape memory alloys (SMAs) have made them valuable engineering materials [1,2]. Industries interested in applying shape memory alloys (SMA) range from automotive to aerospace to microelectronics. Additionally, the excellent biocompatibility of NiTi based SMAs makes them increasingly sought-after for numerous biomedical applications [3–6]. Devices implementing SMA's are becoming increasingly complex and smaller. This requires various laser modification techniques designed to combine different SMA properties into one system [7–10].

Prior studies examining effects of laser processing on the corrosion performance of NiTi SMAs have reported different, and sometimes contradictory, findings. Several publications have shown corrosion performance of NiTi to improve significantly after laser processing [11–13], while some publications report only marginally better performance [14,15]. In contrast, publications have also shown reduced corrosion performance as compared to the original base material [16,17]. Only a few of these studies attempt to characterize the surface after laser processing to determine how the oxide has changed to confirm the mechanisms behind these changes in corrosion performance [12,16,17] and very little research has been done to restore the corrosion performance to pre-processed conditions. For example, Cui et al. [13] characterized

mechanically polished NiTi before and after laser processing by XPS and cyclic polarization. They found that laser processing increased the percent of Ti oxide present on the surface which increased corrosion resistance. Chan et al. [17] also characterized NiTi after laser processing by XPS and cyclic polarization, but they found little compositional differences between the processed region and the base material with only a slight decrease in the corrosion performance. However, another study by Chan et al. [16] observed grain recrystallization in the heat affected zone (HAZ) after laser processing; leading to decreased corrosion resistance in the HAZ region. They also observed that the corrosion performance was enhanced slightly due to an increase in the thickness of the oxide layer [17]. However, this post-process heat treatment was only tested on the base material or weld zone separately, never in a combined system, neglecting the corrosion performance in the heat affected zone (HAZ). In a study by Pequegnat et al. [18] preferential corrosion was observed adjacent to overlapping pulsed laser spots. Therefore, it is necessary to determine what factor leads to these differing results in corrosion performance.

In order to assess the reported discrepancies in corrosion performance after laser processing of NiTi, [13,16,17] we provide an in-depth study that tracks the surface oxide evolution after pulsing with a Nd:YAG laser. Individual laser spots with increasing numbers of pulses were examined to determine how increasing the total energy input to the work material alters the local surface oxide properties. The topography variations were analyzed by optical profilometry whereas the localized corrosion performance of the oxide layer was quantified by scanning electrochemical microscopy (SECM) and surface morphology

---

* Corresponding author.
E-mail address: a2michae@uwaterloo.ca (A. Michael).

was analyzed by X-ray photoelectron spectroscopy (XPS) and Raman spectroscopy. Potentiodynamic cyclic polarization testing was performed on samples processed with overlapping spots, which provided a large enough surface area to properly determine the overall corrosion performance of the laser pulse material and the ability of post-process surface treatments to restore corrosion resistance.

2. Experimental section

2.1. Sample preparation

This study used 0.37 mm thick by 12 mm wide SE508 NiTi strip commercially available through Nitinol Devices and Components (NDC) Incorporated. The nominal chemical composition was 55.8 wt% (50.7 at.%) Ni and 44.2 wt% (49.3 at.%) Ti with a maximum O and C content of 0.05 wt% and 0.02 wt%, respectively, as reported by the manufacturer. Prior to testing, the NiTi strip was ultrasonicated in a 7.5 vol% HF, 20 vol% HNO_3, bal. H_2O solution for 2 min, flipping half way, to remove the thick black oxide layer that forms during manufacturing. After chemically etching, the cross-sectional thickness was measured to be 0.35 mm. For the remainder of this study, the chemically etched state is referred to as 'CE.'

A LW50A Miyachi Unitek pulsed Nd:YAG laser system with a 1.06 μm wavelength, 600 μm nominal spot diameter was used in this study. A flow rate of 14.2 L min^{-1} (30 CFH) of argon shielding gas was found to be sufficient to prevent excessive oxidation of the sample. The CE strip was cleaned with acetone, ethanol, and then de-ionized water prior to laser processing to remove any potential surface contaminants. A pulsed laser profile with a peak power of 0.8 kW for 6 ms followed by a linear ramp down to 0.0 kW over 4 ms was used [10,18].

The laser spots were pulsed one, three and five times to investigate the change in surface reactivity with increased laser pulsing. This material state will be referred to as the "laser processed" (LP) state for the remainder of this study with a number preceding 'LP' indicating number of pulses used. Additional samples were processed such that each spot was pulsed 5 times, with consecutive spots overlapping by approximately 50% to eliminate gaps between spots, as shown in Fig. 1. This melts the sample to a depth of ~300 μm and alters the local composition, as was shown in a previous study [18]. These samples were made to test the effectiveness of post-process surface treatments to restore corrosion resistance. This material state will be referred to as the "laser pulsed" (LP) state for the remained of this study. After laser processing, samples were cleaned again with acetone, ethanol and de-ionized water prior to any testing or post-processing treatments to remove any surface deposits from laser processing.

Some of the overlapped LP samples were treated after laser processing to restore the corrosion resistance. First, a mechanically polished surface was tested to determine if the reduced corrosion performance
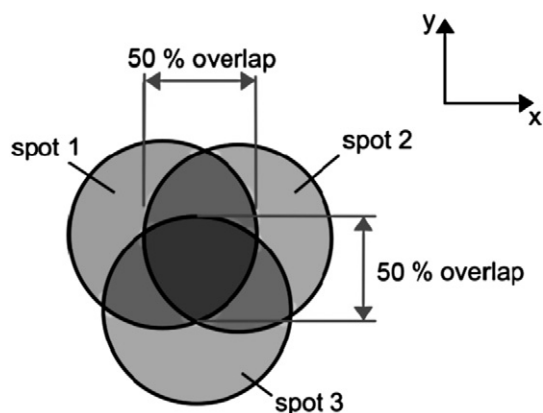

Fig. 1. Illustration of laser spot configuration with 50% overlap.

was a result of the surface morphology or the change in composition. After laser processing, strips were cut in 8 × 8 mm² pieces and progressively ground with 600, 800, 1200 coarse, and 1200 fine grit silicon carbide paper. Polishing was then performed with a 0.03 μm colloidal silica suspension and 30% hydrogen peroxide mixture (9:1 ratio). Extreme care was taken to use consistent grinding/polishing protocol for each individual specimen. This material state will be referred to as the "laser processed and mechanically polished" (LPMP) state for the remainder of the study. The second post-process treatment tested was chemically etching. The samples were immersed in a mixture of 15 vol% HF, 40 vol% HNO_3, and 45 vol% de-ionized water for 30 s, and then immediately ultrasonicated in de-ionized water for 10 min. This material state will be referred to as the "laser processed and chemically etched" (LPCE) state for the remainder of the study.

2.2. Instruments and procedures

The surface topography was characterized using the Nanovea ST400 Optical Profilometer, which is a 3D non-contact profiler that was not affected by sample reflectivity. This is important due to the variation in reflectivity across the sample surface from retained base material to laser spots. Three-dimensional topographical surface maps of the samples were obtained by rastering the optical pen over a 1.2 × 1.2 mm² area using a step size of 5 μm. High-magnification optical microscopy was done with an Olympus BX51M upright inspection and research microscope. Low-magnification optical microscopy was performed on a Leica A60 S Stereomicroscope and a PAX cam LM2 digital camera using Seagull image capture software.

The SECM experiments were carried out using a HEKA scanning electrochemical microscopy (model ELP3, HEKA Electronik, Germany). The laser processed NiTi sample was fixed to the bottom of a Teflon cell. A 25 μm diameter platinum microelectrode (ME) was used as the working electrode. A chloridized silver wire served as a quasi-reference electrode (Ag|AgCl-QRE) and a 0.5 mm diameter platinum wire was used as a counter electrode (Goodfellow Cambridge Limited, Huntingdon, England). MEs were fabricated in-house by sealing Pt wires (25 μm diameter, Delta Scientific Laboratory Products Ltd., Canada) into borosilicate glass capillaries with an outer diameter of 1.5 mm and an inner diameter of 0.7 mm (Sutter Instrument, USA). The probe tip was subsequently sharpened to a ratio $RG = r_{glass} / r_T \approx 10$, where r_{glass} is the radius of the insulating sheath and r_T is the radius of the active ME. The resulting Pt MEs were polished on a microcloth pad (Struers MD Chem cloth) using a series of water-based alumina slurries (i.e. 1 μm, 0.3 μm and 0.05 μm). The working solution was composed of 1 mM FcMeOH as redox-active mediator and 0.1 M K_2SO_4 as the supporting electrolyte in ultra-pure water (Millipore MilliQ water 18.2 MΩ).

SECM feedback images (1.2 × 1.2 mm² area) were acquired with the ME probe positioned at a tip to substrate distance of 10 μm relative to highest topography feature on the surface and using a x, y-scan rate of 5 μm s^{-1}. SECM quantitative feedback approach curves used a z-scan rate of 2 μm s^{-1}. During imaging and acquisition of quantitative feedback approach curves in 1 mM FcMeOH/0.1 M K_2SO_4 solution, the NiTi was not polarized. The ME was polarized at $E_T = 0.4$ V vs Ag|AgCl-QRE to oxidize FcMeOH at a mass-transfer limited rate. The diffusion coefficient D of the redox-active mediator was experimentally determined to be 7.6×10^{-6} cm² s^{-1}.

X-ray photoelectron spectroscopy (XPS) was conducted using a K-Alpha XPS manufactured by ThermoFisher Scientific using monochromatized Al Kα1 radiation. The source was run at 50 eV with a spot size of 30 μm. Survey scans were taken at a pass energy of 200 eV and a binding energy range of 0–1300 eV. The Raman spectrometer used for this experiment was a Renishaw Raman Microscope with a resolution of ≤1 cm^{-1}. The spectra were obtained with a He-Ne laser operating at 633 nm with an incident power of 7.5 mW and a 5 μm spot size. The spot size reported is the focal spot size of the laser used

in this study. The integration time for all Raman spectra is 10 s. The wavelength calibration was made using the silicon emission line at 520 cm^{-1}. Raman spectra were replicated four times with good repeatability for each surface condition.

Potentiodynamic cyclic polarization tests were performed in a phosphate buffered saline (PBS, pH 7.4, MP Biomedicals) electrolyte. Using PBS for cyclic polarization testing is common [18–21], and B.G. Pound [22] has shown that the breakdown potentials of NiTi in PBS are similar to Hanks' solution. Controlling and recording the test was done with a GAMRY Instruments potentiostat using Framework v4.35 software. A 250 mL double walled corrosion cell with a three-electrode configuration was used per the ASTM F2129-08 standard [23]. A saturated calomel electrode (SCE) was used for the reference electrode and a Pt mesh was used for the counter electrode. All potentials in this study will be presented with respect to SCE. The working electrode consisted of an exposed area of the specimen (0.25 cm^2) using an area limiting gasket in a custom holder. Tests were performed at 37 °C to simulate biological conditions. The solution was de-aerated with nitrogen for 30 min before the tests were initiated. The open circuit potential (OCP) was measured until it was stable within 0.05 mV s^{-1}, for a maximum of 1 h. Testing was performed at a scan rate of 0.167 mV s^{-1} per the ASTM G61-86 [24], starting at −600 mV and increasing to 1400 mV, automatically reversing if the current density exceeded 0.1 mA/cm^2. Five specimens were tested for each material condition and representative curves are provided.

3. Results and discussion

In this comprehensive study, the results presented were obtained from experiments designed to thoroughly discover the localized surface conditions of the CE and LP samples, followed by the resulting corrosion performance of CE and LP samples, and finally the effect of post-process surface treatments. First, the surface reactivity was characterized by SECM to identify localized regions of increased reactivity after laser processing. Next, the surface constituents were characterized by XPS and Raman spectroscopy to identify the species present and the degree of crystallinity. Finally, the overall corrosion performance was evaluated using cyclic potentiodynamic polarization testing.
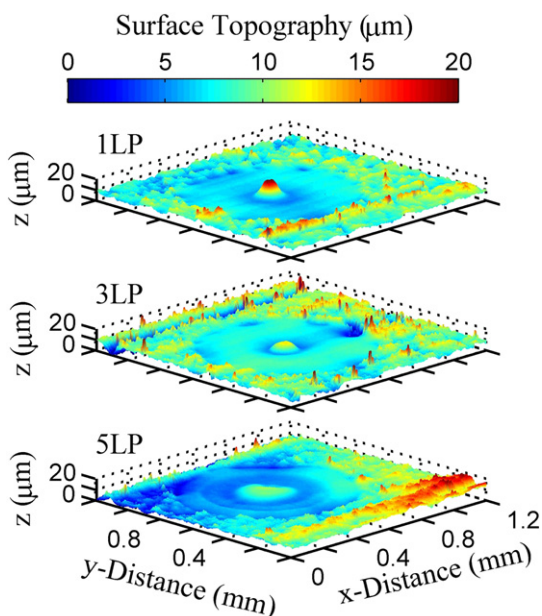

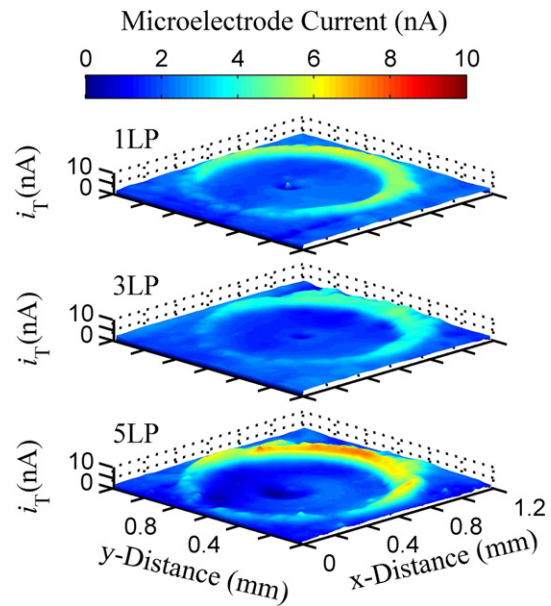**Fig. 2.** Surface topography maps of 1LP, 3LP, and 5LP.

Fig. 3. SECM feedback images 1LP, 3LP, and 5LP.

3.1. Surface morphology and reactivity

The 3D topographical profiles of the individual spots are shown in Fig. 2. The surface roughness values (Ra) values were calculated to be 1.45 μm (1LP), 1.71 μm (3LP), 2.54 μm (5LP). The surface roughness values of all the LP samples were comparable to the roughness value of the CE surface (2.18 μm); however, the laser spots were found to be smoother than the chemically etched material surrounding it. This result is similar to the findings of other laser processing studies [12]. There was a slightly elevated region in the centre of all the spots. This is due to the pressure drop associated with keyhole-mode laser processing. Ripples were also observed in the re-melted region, which increase in intensity with the number of pulses. Analyzing surface morphology prior to SECM analysis was crucial to ascertain the extent that the surface topography affects the SECM feedback measurements.

Fig. 3 shows the SECM images of the NiTi sample surfaces recorded in the feedback mode in a solution containing 1 mM FcMeOH/0.1 M K$_2$SO$_4$. When positioned in the bulk solution (>1 mm from the substrate) a steady state limiting current of 3.15 nA was recorded. It was observed that CE/re-melted regions of the NiTi surface provide small ME current and that of the HAZ region provide a large current response, with a measured current in excess of the bulk solution. In the centre of the laser spots, located at approximately 0.60 mm by 0.65 mm (x, y) topography variations on the order of 7 μm are present in the topography

Table 1
Species identified via XPS analysis on the CE, LP, Edge of spot and LP-Pol surfaces and their respective binding energies (eV).

	Peak energy (eV)	Constituent	Region		
			CE	LP	HAZ
Ni	852.68	Ni 2p2/3	No	Yes	Yes
	855.66	Ni$_2$O$_3$	No	No	Yes
	859.51	Ni 2p2/3	No	No	Yes
Ti	454.85	Ti 2p2/3	No	Yes	No
	458.76	TiO$_2$ 2p2/3	Yes	Yes	Yes
	460.48	Ti 2p2/3	No	No	No
	464.40	TiO$_2$ 2p2/3	Yes	Yes	Yes
O	530.24	TiO$_2$	Yes	Yes	Yes
	532.40	C=O, C—O, HO—Ti—OH	Yes	Yes	Yes

map (Fig. 2). The general patterns observed in the SECM images (Fig. 3) are consistent with the topography images, and the current variations reflect the combined effect of reactivity and topography at the centre of the spot.
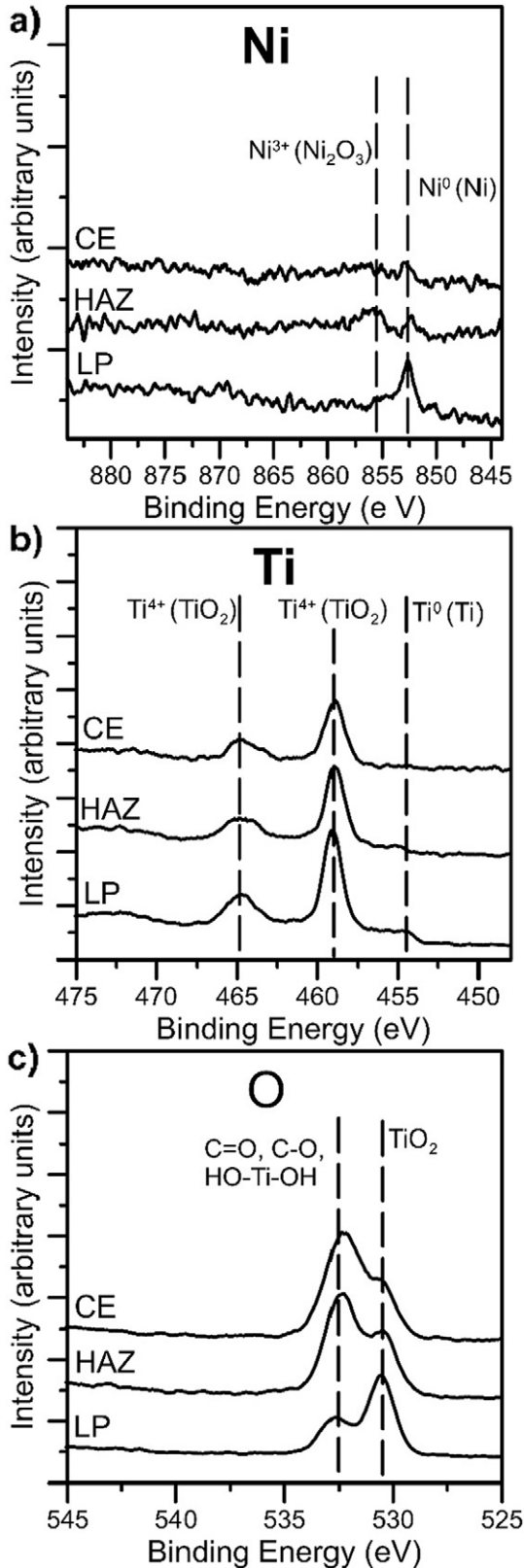

Fig. 4. XPS spectra of Ni, Ti and O from the 5LP sample in the retained CE region, inside the LP region and the HAZ region prior to corrosion testing.
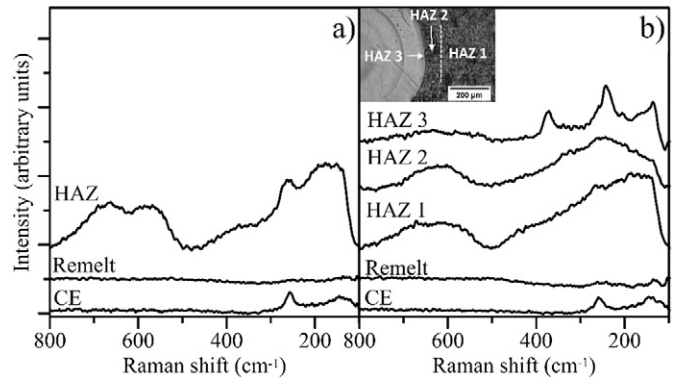

Fig. 5. Raman spectra for a) 1LP and b) 5LP. Inset shows the area from which the Raman spectra were taken, indicating the different HAZ regions observed on 5LP.

3.2. XPS and Raman spectroscopy

The SECM mapping of the laser spot (Fig. 3) was used to direct the XPS and Raman analysis to determine what compositional and structural differences exist between the oxides present in the HAZ, CE and LP regions. First, XPS results for each of the regions in 5LP samples were analyzed and the identified species and their respective binding energies are summarized in Table 1 to aid in further discussion.

Fig. 4 shows the XPS spectra of 5LP NiTi sample in the retained CE region, inside the LP region and the HAZ region prior to corrosion testing. Analysis showed the retained CE and the HAZ regions contained trace amounts of elemental Ni. Additionally, in the HAZ region, Ni_2O_3 was also identified, which is in agreement with previous studies [18]. Although a binding energy of 855.66 eV can be associated with constituents other than Ni_2O_3, laser processing is known to deposit a black plume on the surface [10], which suggests that it is in fact Ni_2O_3. Both the retained CE and HAZ regions contained titanium primarily in the form of TiO_2, with relatively higher intensity in the HAZ region. In these regions, oxygen was mostly in the form of carbon bonding or possible metallic hydroxides with some metallic oxide (TiO_2). XPS analysis inside the LP region showed a greater amount of Ni and Ti compared to the retained CE and HAZ regions. This may be due to the presence of inclusions, such as TiC and Ti_2NiO_x, in the CE and HAZ regions, which would be the result of the material manufacturing process [15]. Similar to the retained CE and HAZ regions, the region inside the LP also contained titanium primarily in the form of TiO_2. Additionally, the
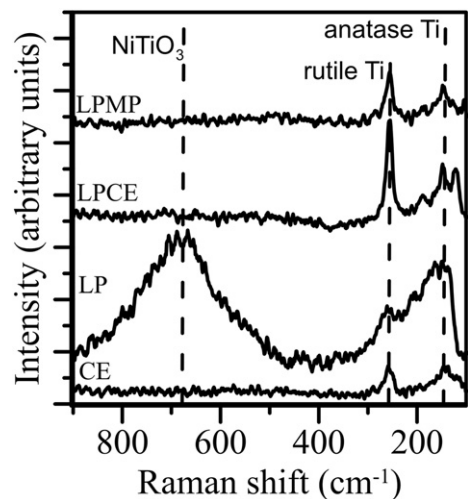

Fig. 6. Representative Raman spectra for the CE surface and untreated HAZ region compared with LPMP and LPCE surfaces.
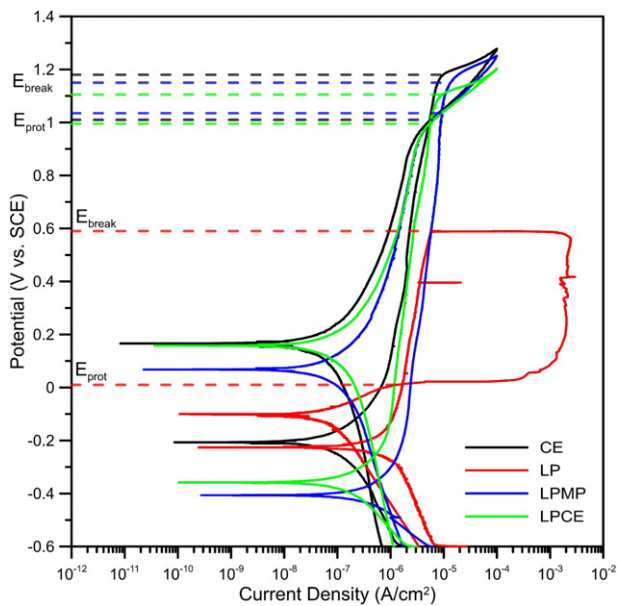
Fig. 7. Representative potentiodynamic cyclic polarization curves comparing CE, LP, LPMP and LPCE.

presence of metallic Ti can be observed inside the LP region at a binding energy of 454 eV. In this region oxygen was mostly in the form of metallic oxide (TiO_2), with some carbon bonding or possible metallic hydroxides.

The Raman spectra for 1LP and 5LP samples are shown in Fig. 5. The 1LP sample had only one distinct HAZ region where partial crystallinity was observed. Due to the broadness of the peaks, the exact species present could not be verified, but the peaks present on the HAZ of the 1LP sample correspond closely with the anatase and rutile forms of TiO_2, which correlates with previous findings [25,26]. The Raman spectrum of outer HAZ region of the 5LP sample, labelled HAZ 1 in Fig. 5b, was similar to the HAZ region observed in the 1LP sample. The inner HAZ region, labelled HAZ 3 in Fig. 5b, displayed significantly sharper peaks, suggesting an increase in crystallinity and/or oxide thickness. The peaks observed in the HAZ 3 tend to correspond more closely to $NiTiO_3$, which has several peaks including ~250 cm^{-1} and ~350 cm^{-1} [26]. However, the absence of a peak above 700 cm^{-1} suggests the presence of Ni_2O_3. The XPS analysis shown in Table 1 also confirms the presence Ni_2O_3. This is an indicator that some form Ni or Ni oxides may have been entrapped in the HAZ region after repeated pulsing. This result correlates well with the SECM maps in Fig. 3, which showed increased reactivity on the right side of the laser spot corresponding to Ni plume deposits. The region labelled HAZ 2 appears to be a transition from the outer HAZ region to the inner HAZ region.

Fig. 6 compares the Raman spectra for LPMP and LPCE with the baseline CE and unfavourable HAZ region from the LP samples. The HAZ region examined on the LP samples was comparable to the HAZ regions observed in the 1LP and 5LP samples. After mechanically polishing, the degree of crystallinity is reduced and comparable to the original CE surface. After chemical etching, the LPCE surface does not show any trace of Ni based crystals; however, the Ti oxide peaks shows an increase in intensity compared the original CE surface. This may be an

indication that some areas on the surface are close to being over etched, as it was etched both before and after laser processing. Potentiodynamic cyclic polarization tests were performed to determine the effect of this crystallinity on the stability of the surface oxide.

3.3. Potentiodynamic cyclic polarization curves

Representative cyclic polarization curves for CE, LP, LPMP and LPCE surfaces are shown in Fig. 7. The current densities in the passive region (i_{pass}) for all materials are of the same magnitude, ranging from 1.99×10^{-6} A/cm^2 to 4.56×10^{-6} A/cm^2. However, the LP and LPMP samples tended to be slightly higher, indicating a marginally faster rate of metal dissolution.

It is important to note that the breakdown (E_{break}) and repassivation (E_{prot}) potentials for the LP sample are drastically lower than all of the other samples. This is not an anomaly, but a manifestation of the instability of the surface oxide after high-energy-input laser processing, and is consistent with results observed by Chan et al. in a previous study [17]. Sudden spikes were also observed in the LP curve, which is likely due to the sudden pitting and repassivation of the material. This was the only sample that experienced this phenomenon and it is most likely related to the instability of the surface oxide after high-energy-input laser processing. After mechanical polishing, E_{break} and E_{prot} are restored to 1137 mV vs SCE and 1026 mV vs SCE, respectively, similar to the 1170 mV vs SCE breakdown potential and 1027 mV vs SCE repassivation potential of the CE surface; however, the corrosion potential (E_{corr}) of the LPMP surface decreases significantly to −461 mV vs SCE compared to −194 mV vs SCE of the CE surfaces. After chemically etching, E_{break} and E_{prot} improve to 1092 mV vs SCE and 974 mV vs SCE, respectively, which is only slightly lower than the breakdown and repassivation potentials of the original CE surface. Again, the E_{corr} of the LPCE sample is reduced to −319 mV vs SCE. The lowering of the corrosion potential for both of the post-processed surfaces indicates that they have a more reactive starting surface. All pertinent values are summarized in Table 2.

A large hysteresis between the breakdown potential and the corrosion potential was observed for the LP sample (570 mV). This large hysteresis has been observed previously from laser welded NiTi [17] and is an indication of a significant loss of material. Both of the post-process treated surfaces had somewhat reduced hystereses on average (LPMP 111 mV and LPCE 118 mV) compared to the original base material (147 mV). This is a good indication that the treatments were effective at restoring the corrosion performance of the laser processed NiTi.

4. Discussion

4.1. Effects of laser processing on surface structure

The corrosion performance of NiTi SMAs is linked to the surface composition and chemistry, surface roughness and homogeneity [8,27, 28]. Laser processing has been found to have a detrimental effect on these properties in some cases [16–18]. It is therefore necessary to discuss the evolution of the surface oxide during laser processing and how post-process surface treatments alter the surface oxide so that corrosion performance of laser processed NiTi may be optimized.

Localized surface reactivity gives great insight into how the surface oxide changes during laser processing. It was observed that after only

Table 2
Corrosion properties measured by potentiodynamic cyclic polarization testing.

Surface	E_{corr} (mV vs SCE)	E_{break} (mV vs SCE)	E_{prot} (mV vs SCE)	i_{pass} (A/cm^2)
CE	−194 ± 32	1170 ± 25	1027 ± 18	2.48 ± 0.55 × 10^{-6}
LP	−250 ± 16	535 ± 71	−35 ± 57	4.56 ± 0.55 × 10^{-6}
LPMP	−460 ± 46	1137 ± 42	1026 ± 7	3.96 ± 0.75 × 10^{-6}
LPCE	−319 ± 27	1092 ± 7	974 ± 17	1.99 ± 0.28 × 10^{-6}

one laser pulse a ring of increased reactivity existed adjacent to the re-melted region (vide infra), see Fig. 3. This corresponds with the heat affected zone (HAZ) found around the weld pool region and was consistent with the studies by Chan et al. [16] and Pequegnat et al. [18] who observed preferential corrosion adjacent to pulsed laser spots. Increasing the number of pulses not only increases the intensity of ME current, it also increases the area in which higher current was observed, as shown in Fig. 8. The high current areas were estimated to be 0.27 mm^2 for 1LP, 0.30 mm^2 for 3LP and 0.40 mm^2 for 5LP.

However, the growth of the annular region of higher ME current was not uniform (Figs. 3) suggesting that it may not result entirely from the formation of the HAZ region. The trailing edge to the right of the re-melted region, see Fig. 3, corresponds to the plume deposits that form on the surface during laser processing, as is clearly observed in the optical image of the laser spot prior to cleaning, as shown in Fig. 9a. This agrees with previous studies that observed Ni-enriched plume deposits after laser pulsing of NiTi SMAs [10]. Note the removal of the black plume deposit to the right of the laser spot after cleaning (Fig. 9b) prior to SECM analysis.

To investigate the effects of the HAZ and nickel plume deposits better XPS analysis was performed to determine which species were present and Raman spectroscopy was performed to determine the degree of crystallinity. The XPS and Raman results confirmed the presence of Ni based oxides in the HAZ region after laser processing. Additionally, the spread of the crystalline structure and the extent to which it crystallizes seems to increase with the number of pulses. This makes sense, as more pulses input more energy into the sample, the oxide crystals are able to grow bigger and further. Thermodynamics of solid state diffusion tells us that when sufficient energy is applied preferred crystal orientations will grow and absorb smaller crystals in order to reduce the overall energy of the crystalline structure. This is the concept applied when metals are annealed. It is well known that welding methods, including pulsed laser methods, provide enough energy for crystal growth to occur in the heat affect zone (that is the definition of a heat affected zone). If one laser pulse provides enough energy for crystals to grow in the HAZ, then multiple pulses will provide enough energy for crystals to grow multiple times.

The presence of these semi-crystalline regions surrounding the pulse is significant in two ways. Firstly, these crystal structures are known to provide a pathway for oxygen to reach the bulk NiTi material below the protective oxide and for Ni to reach the outer surface [25]. This agrees with the SECM findings that showed increased conductivity in the HAZ region. It is well known that an amorphous oxide layer is more robust than a crystalline oxide layer [28,29], since the amorphous oxide lacks these quick diffusion pathways. Secondly, these semi-crystalline regions create non-homogeneity across the surface. It is also well known that a uniform, homogeneous surface oxide is more stable than a heterogeneous surface oxide layer [28].

4.2. Effects of post-process treatment on restoring corrosion properties

Even though laser processing can increase the crystallinity of the surface oxide in the HAZ region, Raman spectroscopy showed that the post-process treatments successfully removed this detrimental crystallinity. The method of mechanically polishing the surface physically removed the old surface oxide layer and rebuilt a new one. The method of chemically etching the surface preferentially removed the Ni ions and oxides present and built up the Ti oxide [29,30].

There was a significant decrease in the corrosion potential, from −194 ± 32 mV vs SCE to −460 ± 46 mV vs SCE, after mechanical polishing for two primary reasons: (i) an increase in elemental Ni composition and (ii) the presence of elemental Ti. The mechanically polished surface contains more elemental Ni compared to the CE surface because this method does not preferentially remove Ni, whereas chemically etching does preferentially remove Ni from the surface. The Ti is only partially oxidized at room temperature so there is still some

elemental Ti in the surface oxide of the LPMP sample [28]. This slight increase of Ni on the surface may also account the increase in the passive current densities of the LPMP (i_{pass} 3.96 × 10^{-6} A/cm^2) and the LP (i_{pass}
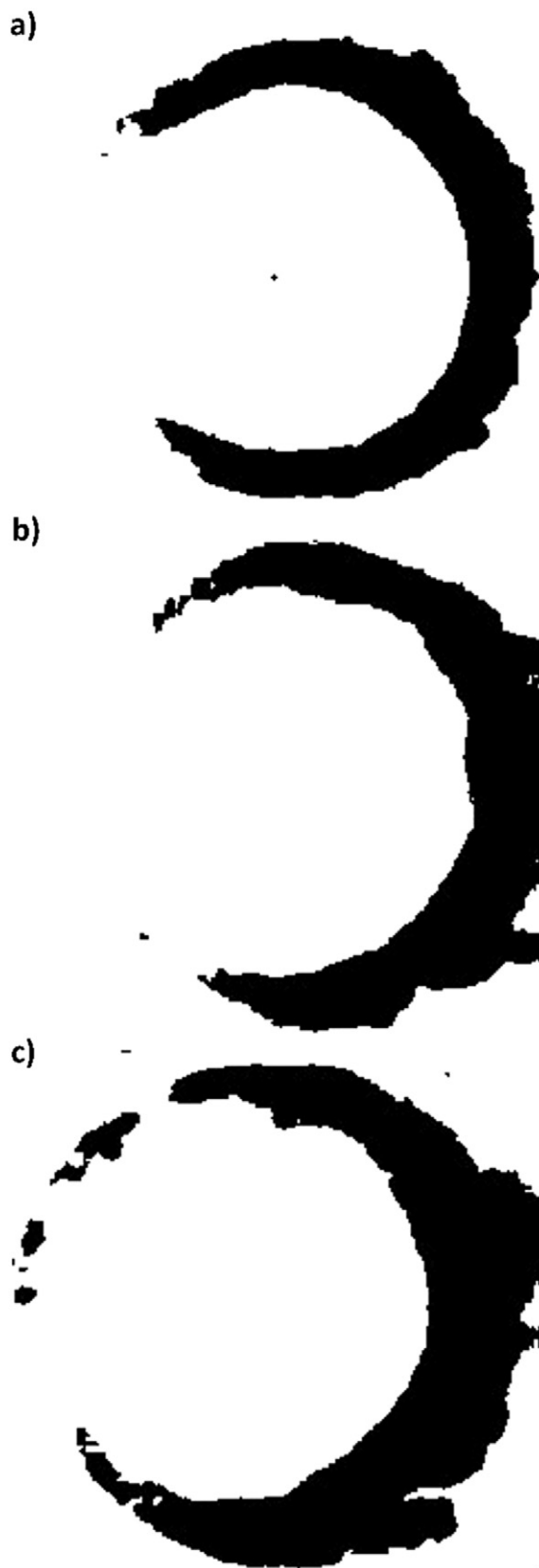

Fig. 8. Surface areas of reactive regions estimated from SECM mappings for a) 1LP, b) 3LP, and c) 5LP. Black regions are conductive areas, white regions are insulating areas.
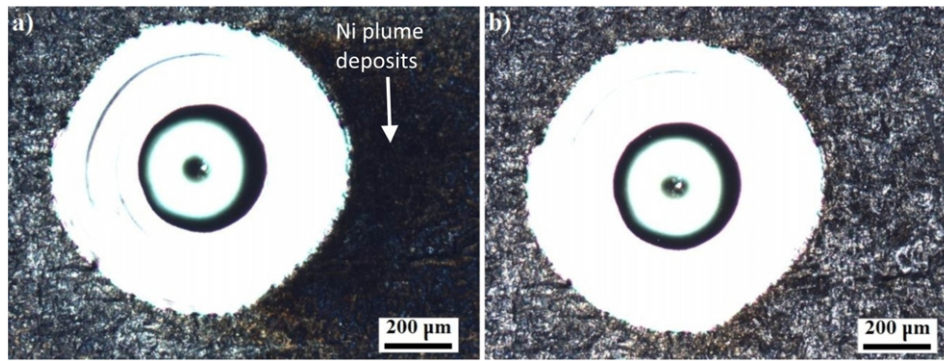
Fig. 9. Optical images of a laser processed sample a) with post-process plume deposits on surface and b) after cleaning thoroughly with acetone, ethanol, and de-ionized water.

4.56×10^{-6} A/cm^2) samples compared to the CE (i$_{pass}$ 2.48×10^{-6} A/cm^2) and the LPCE (i$_{pass}$ 1.99×10^{-6} A/cm^2) samples. It has been shown that there is slow selective dissolution of Ni in the passive region [31].

There was also a marginal difference observed in the breakdown and repassivation potentials between the original chemically etched surface (E$_{break}$ 1170 ± 25 mV vs SCE, E$_{prot}$ 1027 ± 18 mV vs SCE) and the post-processed chemically etched surface (E$_{break}$ 1092 ± 7 mV vs SCE, E$_{prot}$ 974 ± 17 mV vs SCE). This may be because the post-process etching time was significantly shorter in duration than the original etching treatment. This shorter etching time was used to avoid over etching the retained original CE surfaces, which could lead to hydrogen embrittlement [32]. A slight increase in the oxide peak observed by Raman spectroscopy (see Fig. 6) reveals that is was a valid concern, because increasing the crystallinity of Ti can lead to brittleness [33]. The shorter etching time may also have resulted in the decrease of the corrosion potential from -194 ± 32 mV vs SCE to -319 ± 27 mV vs SCE. In the regions where the detrimental Ni oxides were removed, a new Ti oxide was created. With the shorter etching time, the oxidation may have been incomplete in these areas, causing the surface to be more reactive than the original CE surface.

Additionally, an increase in the surface roughness of the LPCE surface compared to the CE surface increases the number of initiation sites for corrosion to occur. Even after the post-process chemical etch, this increased roughness could contribute to the observed disparity in breakdown potentials of the original CE surface and the post-processed CE surface. The 3D topographical profiles for post-process surface treatments are shown in Fig. 10.

Both the LPMP and CE surfaces had comparable breakdown and repassivation potentials. A previous study by Pequegnat et al. [18] showed that the oxide thickness of the mechanically polished surface is about half the thickness of the chemically etched surface. However,

the oxide layer of a MP sample continues to develop in situ [27] preventing earlier failure due to a thinner oxide. It is important to note that the mechanically polished surface does not undergo any preferential corrosion due to the differences in the bulk compositions. This result aligns with the work of Ruhlig et al. [34] who found no significant difference in corrosion performance across the surface of a polished cross-section of a NiTi weld.

Both the mechanically polishing and chemically etching post-process surface treatments were able to restore the corrosion performance of the NiTi SMA to pre-processed capabilities. This shows that any detrimental effects due to laser processing of NiTi SMA are superficial and can be easily removed; however, the optimization of the post-process treatment methods is still required in order to achieve even better corrosion performance.

5. Conclusions

In this study, the evolution of the surface reactivity, crystallinity, and overall oxide stability were characterized after laser processing. It was also demonstrated how post-process surface treatments can remove the surface oxide crystallinity that forms during laser processing of NiTi SMA. The most significant findings of this study included:

1. An increase in surface reactivity was observed in the HAZ region by SECM. It was determined to be a result of increased crystallinity with possible contributions from Ni plume deposits following the heating/cooling cycles that occur during laser processing.
2. The degree of oxide crystallinity increased when the amount of laser pulses increased. The additional heat input from multiple pulses allowed for more crystalline oxide growth.
3. The post-process surface treatments employed were effective at restoring the corrosion performance of laser-process NiTi SMA to pre-
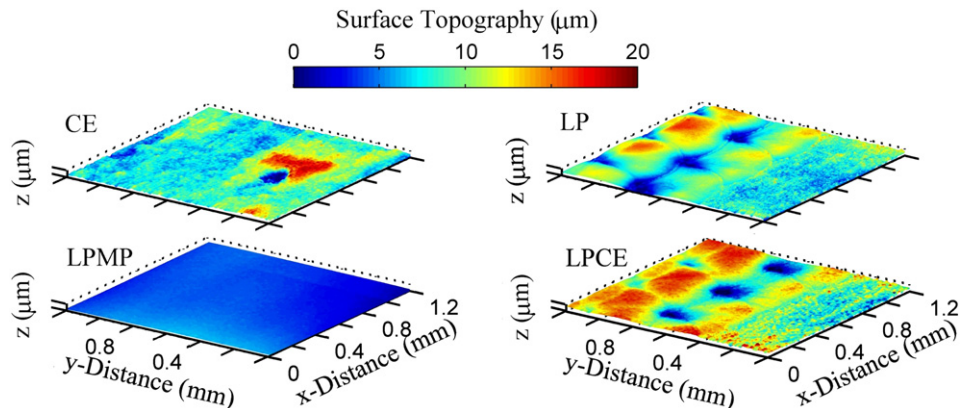

Fig. 10. Surface topography maps of CE, LP, LPMP, and LPCE samples.

processed capabilities. Raman spectroscopy verified the removal of surface oxide crystallinity by both mechanical polishing and chemical etching of the surface of LP samples.

Acknowledgements

References

[1] A.C. Keefe, G.P. McKnight, G.A. Herrera, P.A. Bedegi, Development of a shape memory alloy heat engine through experiment and modeling, Proceedings of the ASME 2011 Conference on Smart Materials, Adaptive Structures and Intelligent Systems, Phoenix, Arizona, USA, 18–21 September 2011, pp. 669–674.

[2] T. Luchetti, A. Zanella, M. Biasiotto, A. Saccagno, Electrically actuated antiglare rear-view mirror based on shape memory alloy actuator, J. Mater. Eng. Perform. 18 (2009) 717–724.

[3] A.R. Pelton, D. Stockel, T.W. Duerig, Medical uses of Nitinol, Proceedings of the International Symposium on Shape Memory Materials, Kanazawa, Japan, May 1999, Materials Science Forum, vol. 327–328, 2000, pp. 63–70.

[4] D. Stockel, A. Pelton, T. Duerig, Self-expanding Nitinol stents: material and design considerations, Eur. Radiol. 14 (2004) 292–301.

[5] T.G. Frank, W. Xu, A. Cuschieri, Instruments based on shape-memory alloy properties for minimal access surgery, interventional radiology and flexible endoscopy, Minim. Invasive Ther. Allied Technol. 9 (2000) 89–98.

[6] J.M. Jani, M. Leary, A. Subic, M.A. Gibson, A review of shape memory alloy research, applications and opportunities, Mater. Des. 65 (2014) 1078–1113.

[7] P. Sevilla, F. Martorell, C. Libenson, J.A. Planell, F.J. Gil, Laser welding of NiTi orthodontic archwires for selective force application, J. Mater. Sci. Mater. Med. 19 (2008) 525–529.

[8] Q. Meng, Y. Liu, H. Yang, B.S. Shariat, T.H. Nam, Functionally graded NiTi strips prepared by laser surface anneal, Acta Mater. 60 (2012) 1658–1668.

[9] M. Daly, A. Pequegnat, Y. Zhou, M.I. Khan, Fabrication of a novel laser-processed NiTi shape memory microgripper with enhanced thermomechanical functionality, J. Intell. Mater. Syst. Struct. 24 (2013) 984–990.

[10] M.I. Khan, A. Pequegnat, Y. Zhou, Multiple memory shape memory alloys, Adv. Eng. Mater. 15 (2013) 386–393.

[11] F. Villermaux, M. Tabrizian, L.H. Yahia, M. Meunier, D.L. Piron, Excimer laser treatment of NiTi shape memory alloy biomaterials, Appl. Surf. Sci. 109 (1997) 62–66.

[12] H.C. Man, Z.D. Cui, T.M. Yue, Corrosion properties of laser surface melted NiTi shape memory alloy, Scr. Mater. 45 (2001) 1447–1453.

[13] Z.D. Cui, H.C. Man, X.J. Yang, The corrosion and nickel release behavior of laser surface-melted NiTi shape memory alloy in Hanks' solution, Surf. Coat. Technol. 192 (2005) 347–353.

[14] X.-J. Yan, D.-Z. Yang, Corrosion resistance of a laser spot-welded joint of NiTi wire in simulated human body fluids, J. Biomed. Mater. Res. A 77A (2006) 97–102.

[15] X.J. Yan, D.Z. Yang, X.P. Liu, Corrosion behavior of a laser-welded NiTi shape memory alloy, Mater. Charact. 58 (2007) 623–628.

[16] C.W. Chan, H.C. Man, T.M. Yue, Susceptibility to stress corrosion cracking of NiTi laser weldment in Hanks' solution, Corros. Sci. 57 (2012) 260–269.

[17] C.W. Chan, H.C. Man, T.M. Yue, Effect of post-weld heat-treatment on the oxide film and corrosion behavior of laser-welded shape memory NiTi wires, Corros. Sci. 56 (2012) 158–167.

[18] A. Pequegnat, A. Michael, J. Wang, K. Lian, Y. Zhou, M.I. Khan, Surface characterizations of laser modified biomedical grade NiTi shape memory alloys, Mater. Sci. Eng. C 50 (2015) 367–378.

[19] N. Munroe, C. Pulletikurthi, W. Haider, Enhanced biocompatibility of porous Nitinol, J. Mater. Eng. Perform. 18 (2009) 765–767.

[20] W. Haider, N. Munroe, Assessment of corrosion resistance and metal ion leaching of Nitinol alloys, J. Mater. Eng. Perform. 20 (2011) 812–815.

[21] C. Liu, P.K. Chu, G. Lin, D. Yang, Effects of Ti/TiN multilayer on corrosion resistance of nickel-titanium orthodontic brackets in artificial saliva, Corros. Sci. 49 (2007) 3783–3796.

[22] B.G. Pound, Susceptibility of nitinol to localized corrosion, J. Biomed. Mater. Res. A 77 (2006) 185–191.

[23] American Society for Testing and Materials (ASTM), Standard Test Method for Conducting Cyclic Polarization Measurements to Determine the Corrosion Susceptibility of Small Implant Devices, Standard F2129-08, ASTM International, West Conshohocken, PA, 2008.

[24] American Society for Testing and Materials (ASTM), Standard Test Method for Conducting Cyclic Potentiodynamic Polarization Measurements for Localized Corrosion Susceptibility of Iron-, Nickel-, or Cobalt-based Alloys, Standard G61-86, ASTM International, West Conshohocken, PA, 2009.

[25] C.L. Chu, C.Y. Chung, P.K. Chu, Surface oxidation of NiTi shape memory alloy in a boiling aqueous solution containing hydrogen peroxide, Mater. Sci. Eng. A 417 (2006) 104–109.

[26] G.S. Firstov, R.G. Vitchev, H. Kumar, B. Blanpain, J. Van Humbeeck, Surface oxidation of NiTi shape memory alloy, Biomaterials 23 (2002) 4863–4871.

[27] O. Cissé, O. Savadogo, M. Wu, L'.H. Yahia, Effect of surface treatment of NiTi alloy on its corrosion behavior in Hanks' solution, J. Biomed. Mater. Res. 61 (2001) 339–345.

[28] S.A. Shabalovskaya, Surface, corrosion and biocompatibility aspects of nitinol as an implant materials, Biomed. Mater. Eng. 12 (2002) 69–109.

[29] S. Shabalovskaya, J. Anderegg, J. Van Humbeeck, Critical overview of Nitinol surfaces and their modifications for medical applications, Acta Biomater. 4 (2008) 447–467.

[30] S. Shabalovskaya, J. Anderegg, F. Laab, P.A. Thiel, G. Rondelli, Surface conditions of Nitinol wires, tubing, and as-cast alloys: the effect of chemical etching, aging in boiling water, and heat treatment, J. Biomed. Mater. Res. B Appl. Biomater. 65 (2003) 193–203.

[31] D.A. Dalla Corte, L.F.P. Dick, Selective dissolution of Ni from Nitinol for increasing biocompatibility, ECS Trans. 11 (2008) 29–30.

[32] K'.I. Yokoyama, Y. Yazaki, J'.I. Sakai, Inhibition of hydrogen embrittlement of Ni-Ti superelastic alloy in acid fluoride solution by hydrogen peroxide addition, J. Biomed. Mater. Res. A 98 (2011) 404–411.

[33] M.H.O. Kononen, E.T. Lavonius, J.K. Kivilahti, SEM observations on stress corrosion cracking of commercially pure titanium in a topical fluoride solution, Dent. Mater. 11 (1995) 269–272.

[34] D. Ruhlig, H. Gugel, A. Schulte, W. Theisen, W. Schuhmann, Visualization of local electrochemical activity and local nickel ion release on laser welded NiTi/steel joints using combined alternating current mode and stripping mode SECM, Analyst 133 (2008) 1700–1706.